In operando Synchrotron Diffraction and *in operando* X-ray Absorption Spectroscopy Investigations of Orthorhombic V_2O_5 Nanowires as Cathode Materials for Mg-Ion Batteries

Qiang Fu[a,*], Angelina Sarapulova[a], Vanessa Trouillet[a,c], Lihua Zhu[a], Francois Fauth[d], Stefan Mangold[e], Edmund Welter[f], Sylvio Indris[a,b], Michael Knapp[a,b], Sonia Dsoke[a,b], Natalia Bramnik[a], Helmut Ehrenberg[a,b]

[a]Institute for Applied Materials (IAM), Karlsruhe Institute of Technology (KIT), Hermann-von-Helmholtz-Platz 1, D-76344 Eggenstein-Leopoldshafen, Germany

[b]Helmholtz Institute Ulm for Electrochemical Energy Storage (HIU), Helmholtzstrasse 11, 89081 Ulm, Germany

[c]Karlsruhe Nano Micro Facility (KNMF), Karlsruhe Institute of Technology (KIT), Hermann-von-Helmholtz-Platz 1, D-76344 Eggenstein-Leopoldshafen, Germany

[d]CELLS-ALBA Synchrotron, E-08290 Cerdanyola del Valles, Barcelona, Spain

[e]Institute for Photon Science and Synchrotron Radiation, Karlsruhe Institute of Technology, Hermann-von-Helmholtz-Platz 1, D-76344 Eggenstein-Leopoldshafen, Germany

[f]Deutsches Elektronen-Synchrotron DESY-A Research Centre of the Helmholtz Association, Notkestraße 85, D-22607 Hamburg, Germany

Corresponding author: qiang.fu@kit.edu (Q. Fu)

Tel: 49-721 608-41445, Fax: 49-721 608-28521.

Abstract:

Orthorhombic V_2O_5 nanowires were successfully synthesized via a hydrothermal method. A cell-configuration system was built utilizing V_2O_5 as the cathode and 1 M $Mg(ClO_4)_2$ electrolyte within acetonitrile, together with $Mg_xMo_6S_8$ ($x \approx 2$) as the anode to investigate the structural evolution and oxidation state and local structural changes of V_2O_5. The V_2O_5 nanowires deliver an initial discharge/charge capacity of 103 mAh g^{-1}/110 mAh g^{-1} and the highest discharge capacity of 130 mAh g^{-1} in the 6^{th} cycle at C/20 rate in the cell-configuration system. *In operando* synchrotron diffraction and *in operando* X-ray absorption spectroscopy together with *ex situ* Raman and X-ray photoelectron spectroscopy reveal the reversibility of magnesium insertion/extraction and provide the information on the crystal structure evolution and changes of the oxidation states during cycling.

Keywords: Orthorhombic V_2O_5 Nanowires; *In operando* Synchrotron Diffraction; *In operando* X-ray Absorption Spectroscopy; Mg-Ion Batteries

1. Introduction

Since the early 1990s, Lithium-ion batteries (LIBs) have been the most significant and widespread used secondary battery. Low-cost, high-safety and high-energy density batteries are highly required and in demand for storage of the intermittent energy from renewable resources, such as solar and wind power. However, the application of LIBs in large-scale energy storage, for instance, power grid, is still limited by the price, resources, and safety issues[1-4]. Because of significantly notable advantages of Mg metal such as the abundant resources, lower cost, high theoretical volumetric capacity (3833 mAh cm^{-3}) and high safety, magnesium-ion batteries (MIBs) have been considered as a very promising alternative to replace LIBs[5-8]. Gregory et al.[9] initiated the usable Mg rechargeable battery systems in the 1980s and they developed the electrolyte solutions containing Mg-organo-borate moieties (the first breakthrough in the field), $Mg(BBu_2Ph_2)_2$ within tetrahydrofuran (THF). Although this electrolyte was capable of the reversible deposition/ dissolution and, therefore, the usage of metallic Mg as an anode, the electrochemical window was narrow (< 2 V). The second breakthrough in this field was done by Aurbach et al. in 2000[10], who introduced the electrolyte solutions formed by the reaction of $AlCl_{3-n}R_n$ Lewis acid with R_2Mg Lewis base in ethers (THF or glymes). Hence, the first rechargeable magnesium battery composed of Mg metal, Chevrel phase cathode, and $Mg(AlCl_2BuEt)_2$ electrolyte was demonstrated. The Mg battery showed excellent cycle life (>3500), low capacity fading with cycling, and very low self-discharge, as well as a wide temperature operating range. Afterward, another advanced electrolyte solution with a wide electrochemical window (>3 V), the all-phenyl-complex (APC) electrolyte, was developed by Aurbach et al.[11]. Despite the potential advantages of Mg and great progress in MIBs, many challenges need to be overcome before the commercialization of MIBs. One of the major issues is the lack of suitable cathode materials and incompatibility of electrolytes with high-voltage cathodes and metallic Mg anodes. Moreover, the most common Mg-ion electrolytes exhibit high corrosion to the battery casing and current collectors. For example, stainless steel would be corroded above 2 V vs Mg^{2+}/Mg within the known APC electrolyte[12]. The amount of promising Mg-insertion materials is also limited due to sluggish Mg-ion solid diffusion in the solids originated from the Mg-ion's divalent character of its high charge density and high Mg^{2+} migration barriers. The high charge density of Mg^{2+} probably contributes to larger desolvation energy of charge transfer at the cathode/electrolyte interface[13-14], which could give a higher

charge transfer resistance and hinder the ion mobility. The rate capability of the Mg-insertion cathodes can be improved to some extent by using nanomaterials, open tunnel structure or employing layered materials[15]. Thanks to their proven high working voltage and high energy density within LIBs, vanadium oxide materials are extremely attractive for MIBs.

Vanadium pentoxide (V_2O_5) has large enough interstitial vacancies to adopt various guest species, such as Li^+, K^+, Na^+, as well as Mg^{2+} [16-18]. For V_2O_5 aerogel, the uptake of 4 mol of Mg^{2+} per mol V_2O_5 was demonstrated in a chemical magnesiation test[19]. In the past ten years, a lot of work[17, 20-28] has been done on the V_2O_5 as cathode materials for MIBs. However, up to now, only limited capacities have been achieved for this kind of cathode material in electrochemical cells with a Mg electrolyte. For instance, Tang and co-workers[17] reported a discharge capacity of 180 mAh g^{-1} for aero-gel V_2O_5 dominated by the surface morphology, such as thin and mesoporous solid phase. Yu and Zhang[20] reported that the electrochemical performance of V_2O_5 in a $Mg(ClO_4)_2$ electrolyte with propylene carbonate (PC) is determined by H_2O content in the electrolyte. The highest first discharge capacity of 158.6 mAh g^{-1} in this study was demonstrated for a 1 M $Mg(ClO_4)_2$ + 1.79 M H_2O/PC electrolyte. Highly reduced VO_x nanotube delivered an initial discharge capacity of 218 mAh g^{-1} in $Mg(ClO_4)_2$/acetonitrile electrolyte, as reported by Kim and co-workers[21]. Very recently, Banerjee et al.[24] reported that a metastable V_2O_5 (ζ-V_2O_5, space group *C*2/*m*) delivered an initial discharge capacity of 140 mAh g^{-1} and retained discharge capacity of 90 mAh g^{-1} after 100 cycles. The V_2O_5 nanoclusters within a porous carbon support with a molecular energy storage mechanism were demonstrated to deliver an initial discharge capacity of 300 mAh g^{-1} in the working potential range of 0.5-2.8 V[25]. Gershinsky et al.[28] reported a reversible capacity of ~150 mAh g^{-1} for V_2O_5 thin film within a working potential range of 2.2 - 3.0 V vs Mg^{2+}/Mg. In Gershinsky's work[28], the weakened intensity of reflections and main reflection shift of 010 to lower angle were observed for V_2O_5 film material via *ex situ* X-ray diffraction (XRD). However, a detailed investigation of structural changes of V_2O_5 in the discharging and charging processes is still missing. *In operando* synchrotron diffraction serves as a highly powerful technique to look into the structural changes of a battery material[29-30]. In order to get a better understanding of the structural evolution of a battery material in "real time", *in operando* synchrotron powder diffraction should be performed. In addition, *in operando* X-ray absorption spectroscopy (XAS) serves as another powerful technique to reveal the local structure and oxidation state during the electrochemical reaction.

Orthorhombic V_2O_5 (α-V_2O_5) has the space group *Pmn*2_1 and it is composed of [VO_5] square pyramid layers connected by sharing edges and corners (distorted) and alternating in an up-up-down-down sequence with every third row being vacant[31]. In addition, there are three different oxygens, O1, O2, and O3, in the structure and the V_2O_5 sheet is held together via a weak vanadium-oxygen interaction, which can provide accommodating interlayer space for the intercalation reactions. Concerning lithium-ion batteries, the structural evolution of orthorhombic V_2O_5 during Li-ion intercalation has been well investigated[4, 32-36]. The α-phase is discovered at $x < 0.1$, and the ε-phase is detected at $0.35 < x < 0.7$, while the δ-phase is obtained at $x = 1$ for $Li_xV_2O_5$. Beyond $x = 1$, an irreversible transformation from δ-phase to γ-phase is observed and the γ-phase is capable of being reversibly cycled for $0 \leq x \leq 2.0$ while remaining within the γ-type structure. The irreversible formation of ω-phase with a rocksalt-type structure emerges upon the third lithium insertion into the V_2O_5 structure. Among these phases, the α-, ε-, and δ-phases composed of [VO_5] square pyramids are orthorhombic with an increased puckering in the layers. The γ-phase is also made up of [VO_5] square pyramids as well, but it is highly puckered and irreversible (metastable γ'-phase upon complete deintercalation), while the ω-phase is tetragonal, which differs greatly from the initial orthorhombic V_2O_5 phase. However, some authors suggested the coexistence of Li_xVO_2 and Li_3VO_4 compounds rather than the γ- and ω-phase[36-37].

To the best of our knowledge, *in operando* techniques have not yet been applied to study the reaction mechanism of V_2O_5 materials in MIBs in detail. In the present work, two strategies are proposed to improve the Mg^{2+} intercalation into the V_2O_5 cathode and to investigate the electrochemical mechanism during cycling: (1) to prepare nanosized V_2O_5 materials. It has been demonstrated, by first-principles calculations, that the diffusion barrier of Mg^{2+} can be reduced to 0.20 eV in single layered V_2O_5[38] and the Mg^{2+} ions' hopping barrier in V_2O_5 is 1.26 eV[39-40], which is 3 times higher than that of 0.35 eV for Li^+ ions. In addition, it is well known that nanosized materials provide short diffusion lengths for cation insertion, which results in higher capacities. Generally, numerous nanostructured vanadium oxide materials as reported in the literature displayed a superior electrochemical performance because of their high specific areas and short Mg-ion migration pathways. (2) to build a cell-configuration system in a chosen "standard" polar aprotic electrolyte. As reported in several publications[9, 41-42], passivation films could be formed on the metal for a vast majority of organic solvents and normal salts, such as carbonates and nitriles, $Mg(SO_3CF_3)_2$ and $Mg(ClO_4)_2$, respectively. The APC electrolyte

developed by Aurbach has an electrochemical window ~3.3 V vs Mg^{2+}/Mg, but it will corrode the stainless steel based cell casing above 2.0 V for V_2O_5. Due to the incompatibility of metallic Mg with chosen "standard" electrolyte, it is necessary to avoid the use of metallic Mg as an anode by adopting a cell-configuration system. In the present study, we studied the electrochemistry of V_2O_5 nanowires in 1M $Mg(ClO_4)_2$ in acetonitrile (AN) electrolyte together with $Mg_xMo_6S_8$ ($x \approx 2$) anode. The evolution of the crystal structure, oxidation state and local structural changes were studied by *in operando* synchrotron diffraction and *in operando* XAS.

2. Experimental

Synthesis of V_2O_5 nanowires: The V_2O_5 nanowires were synthesized via a modified hydrothermal method as reported earlier[43]. Briefly, ammonium metavanadate (NH_4VO_3, 0.3 g), HCl (2 M, 1.0 ml), surfactant P123 ($EO_{20}PO_{70}EO_{20}$, where PO and EO are propylene oxide, and ethylene oxide respectively, 0.5 g) and 30 ml of deionized water were mixed (with ultrasonication for 10 mins) and stirred for 1 h. Afterward, the mixtures were put into 50ml Teflon-lined autoclaves and kept for 24 h at 120 ^oC in an oven. The resultant precipitates were filtered and rinsed three times with distilled water and acetone. The product was annealed at 400 ^oC for 2 h in the air with a heating rate of 10 ^oC/min after drying at 120 ^oC for 24 h under vacuum.

***Synthesis of Mo_6S_8*:** Mo_6S_8 was synthesized according to the reported work[44]. The $Cu_2Mo_6S_8$ was synthesized through a molten salt synthesis using KCl as salt. Typically, CuS (0.398 g), Mo (0.602 g), MoS_2 (1 g), and KCl (2 g) were ground in the glovebox and annealed in an alumina crucible under argon atmosphere. The mixtures were kept at 850 ^oC for 60 h with a ramping rate of 150 ^oC/h and then the furnace was cooled down to the room temperature. The residual salt was washed two times with hot distilled water. Then the powder was put into a 6 M HCl solution with strong stirring for 7 h and bubbled with O_2, which was required to leach Cu and to obtain the Mo_6S_8 product. Finally, the remaining powders were washed with distilled water and dried at 120 ^oC for 2 h.

Preparation of two electrolytes: The preparation of electrolytes was conducted in glove box (Ar atmosphere) with very low H_2O and O_2 ($\leq$2 ppm). APC electrolyte, 0.4 M $(PhMgCl)_2$-$AlCl_3$, was prepared by dissolving a certain amount of aluminium chloride powder ($AlCl_3$) and 2 M

phenylmagnesium chloride solution of tetrahydrofuran $(PhMgCl)_2$/THF in tetrahydrofuran (THF). All these chemicals were water-free grade and purchased from Sigma-Aldrich. A 1 M $Mg(ClO_4)_2$/AN was prepared by dissolving a certain amount of anhydrous $Mg(ClO_4)_2$ (Fox-Chemicals) in anhydrous acetonitrile (Alfa Aesar) with vigorous stirring at room temperature in the Ar-filled glovebox, where $Mg(ClO_4)_2$ and AN are water free without further drying.

Morphological, Structural and Surface Characterization: The morphology of materials was characterized with Zeiss Supra 55 scanning electron microscope (SEM) with primary energy of 15 keV. The structural characterizations were done utilizing synchrotron radiation (λ = 0.4132 Å, 30 keV) at the Material Science and Powder Diffraction beamline (MSPD) at ALBA synchrotron (Barcelona, Spain)[45]. The powder diffraction patterns were collected in capillary geometry with powders filled in 0.5 mm Ø boro-silicate capillaries. Raman scattering of the products was recorded on a microscope type HORIBA LabRam Evolution HR with a laser source (λ = 523 nm, 10 mW) from 100 to 1100 cm^{-1}. The washed and dried electrodes after discharging and charging were sealed in a cell with a quartz window inside a glovebox. The window is suitable for *ex situ* Raman measurement. X-ray photoelectron spectroscopy (XPS) was performed utilizing an XPS spectrometer (K-Alpha$^+$) with a micro-focused, monochromatized Al K_α X-ray source (ThermoFisher Scientific, East Grinstead, UK). The sample storage and transportation for XPS characterization were done in an airtight transport vessel under Ar to the spectrometer. Thermo Avantage software was used to perform data acquisition and processing as mentioned elsewhere[46]. One or more Voigt profiles were used to fit the spectra. The graphite C 1s peak at 284.4 eV binding energy is reference for all spectra, which was controlled employing the peaks of metallic Ag, Cu, and Au, respectively. The binding energy uncertainty of intense peaks was about ±0.1 eV and the uncertainty of weak peaks was estimated to be ±0.2 eV. The Scofield's sensitivity factors[47], analyzer transmission function, and effective attenuation lengths (EALs) for photoelectrons were employed for quantification and the standard TPP-2M formalism was used to calculate the EALs[48].

Electrochemical Characterization: The electrodes were prepared through mixing V_2O_5 nanowires or Mo_6S_8 active material, respectively, with Super C65 (TIMCAL) and polyvinylidene difluoride (PVDF) binder with a ratio of 70:20:10 within N-Methyl-2-pyrrolidone solvent. After drying, the cathode materials (active V_2O_5 of 3.71 mg with total average thickness of 126 μm

and Mo_6S_8 of 11.10 mg with total average thickness of 142 μm) were pressed on a current collector of 12 mm stainless steel mesh with a thickness of 60 μm before assembling the 2-electrode Swagelok cells (modified cell design from our previous work[49], for details see **Fig. S1**). As displayed in **Scheme 1**, before assembling the cell configuration V_2O_5 | $Mg(ClO_4)_2$/AN | $Mg_xMo_6S_8$ (x ≈ 2), a cell consisting of Mo_6S_8 | APC | Mg was made and discharged to obtain the $Mg_xMo_6S_8$ negative electrode. Then, the cell was disassembled and the $Mg_xMo_6S_8$ electrode was washed using THF solvent and dried in the glovebox. In the rebuild V_2O_5 | $Mg(ClO_4)_2$/AN | $Mg_xMo_6S_8$ cell configurations, the mass of $Mg_xMo_6S_8$ was intentionally in excess (10-15 % capacity excess of $Mg_xMo_6S_8$ based on 1 mol of Mg^{2+} per mol V_2O_5). *Note that specific capacities in this work were calculated in terms of the weight of the V_2O_5 active cathode material.* A multichannel electrochemical workstation (Bio-Logic VMP) was used to conduct galvanostatic cycling and cyclic voltammetry (long cycling with a rate of C/20; for *ex situ* Raman and XPS with a rate of C/80).

***Ex situ Raman and ex situ XPS Sample Preparation*:** the rebuild cell configurations, consisting of V_2O_5 and $Mg_xMo_6S_8$ with a $Mg(ClO_4)_2$/AN electrolyte, were disassembled and washed with AN in Ar-filled glovebox for the 1st discharged state at 0.01 V and the 1st charged state at 1.6 V with C/80 rate. (For discharged/charged samples, the active V_2O_5 of 3.185 mg/2.996 mg with total average thickness of ~110 μm and Mo_6S_8 of 9.24 mg/8.939 mg with total average thickness of ~135 μm)

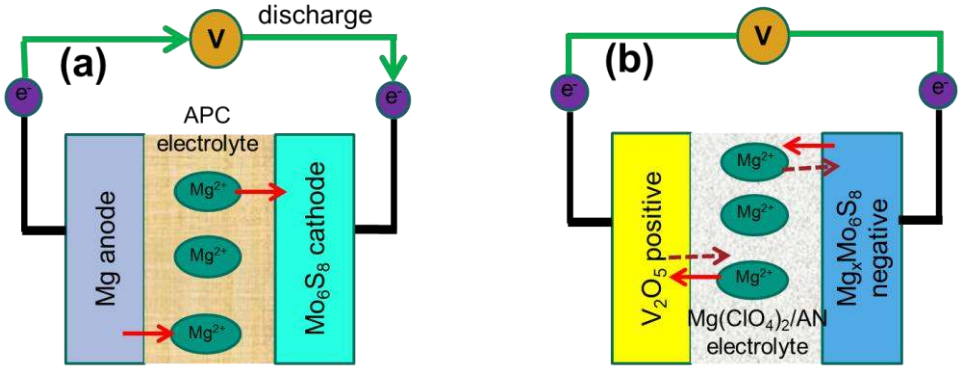

Scheme 1 The compositions of the half-cell for the electrochemical preparation of the $Mg_xMo_6S_8$ anode (a) and V_2O_5 | $Mg(ClO_4)_2$/AN | $Mg_xMo_6S_8$ (x ≈ 2) cell configuration (b)

In operando Synchrotron Diffraction and in operando X-ray Absorption Spectroscopy (XAS): *In operando* synchrotron diffraction during cycling was performed at MSPD at ALBA synchrotron. The *in operando* cells for XRD were built by using 2025-type coin cells with a 5 mm diameter beam entrance covered by glass windows. The cathode material (V_2O_5 mixture, in total 4.4 mg with average thickness of 140 μm) was prepared by pressing the mixture on a stainless steel mesh within a 5 mm hole in the center, and a $Mg_xMo_6S_8$ anode (pure Mo_6S_8 mass: 9.94 mg with total average thickness of 155 μm) was made in the same way, but with a 5 mm hole in the center (**Fig. 1a**). In this way, only the V_2O_5 material will be detected during the *in operando* synchrotron measurements. More details of this setup can be found elsewhere[30]. *In operando* synchrotron diffraction patterns were collected at room temperature and λ= 0.4132 Å wavelength (30 keV), utilizing the position sensitive detector MYTHEN. Data were collected with effective exposure time of 60 s in steps of 0.006° over angular range of 1.8° - 42° in 2theta during the first two cycles with C/25 rate. In order to improve the powder averaging (increasing the number of crystallites contribution), the coin cells were continuously oscillated +/-5 ° around the incoming beam direction.

The diffraction data analysis was carried out by the Rietveld method with applying the Fullprof software package[50]. The same model was used for the Rietveld refinement of Mg-poor and Mg-rich phases with different lattice parameters, where the positions of the Mg ions were clarified by Shklover and Haibach[51]. For the Rietveld refinement, the occupancy of Mg was determined and fixed according to the charge and capacity in the electrochemical data, where x in $Mg_xV_2O_5$ is recorded by EC lab software for each diffraction pattern. *In operando* XAS measurements were conducted at synchrotron at the KIT, Karlsruhe. Photographs and schematic drawing of a modified *in operando* cell set up from our previous work is shown in **Fig. 1b** and **c**[29]. *In operando* XAS measurements were carried out during the first discharge-charge processes with C/25 rate (active V_2O_5 of 3.493 mg with average thickness of 145 μm and pure Mo_6S_8 mass of 10.15 mg with average total thickness of 155 μm). XAS spectra of Vanadium K-edge were recorded in quick-XAS (6 min/spectrum) mode in fluorescence geometry using a germanium detector, since the penetration depth is several μm thick (bulk method), and the chances of a fluorescence photon to reach the detector are excellent. The V K-edge for V_2O_5 was measured during the electrochemical cycling and the energy was calibrated using a vanadium foil as commonly employed in XAS experiments. V_2O_3, VO_2, and V_2O_5 were used as standard materials. All the

data were collected at room temperature with a Si (111) double crystal monochromator and all the XAS spectra were analyzed and processed utilizing the DEMETER software package[52].

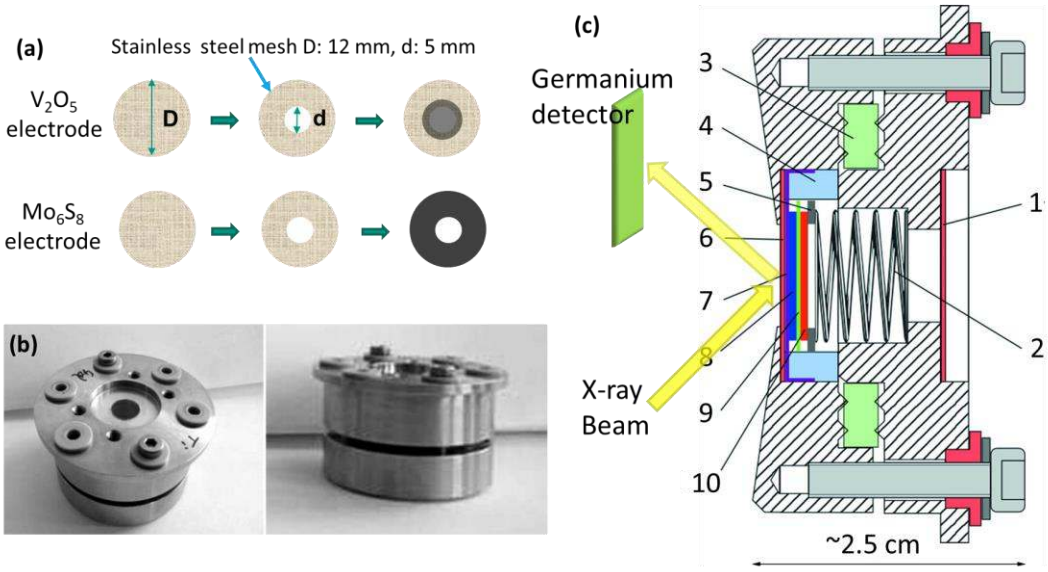

Figure 1 Electrode preparation used for *in operando* cell (a), photographs and schematic diagram of the *in operando* cell design (b, c): (1) and (6) 125 μm Kapton windows, (2) contact spring (stainless steel), (3) plastic sealing ring, (4) insulating PTFE ring, (5) and (7) current collector and current collector of stainless steel mesh with 9 mm hole in the center, (8) working electrode (WE), (9) Whatmann separator, and (10) counter electrode (CE) (modified cell design from our previous work[29]).

3. Results and Discussion

3.1 Structural and Morphological Characterization

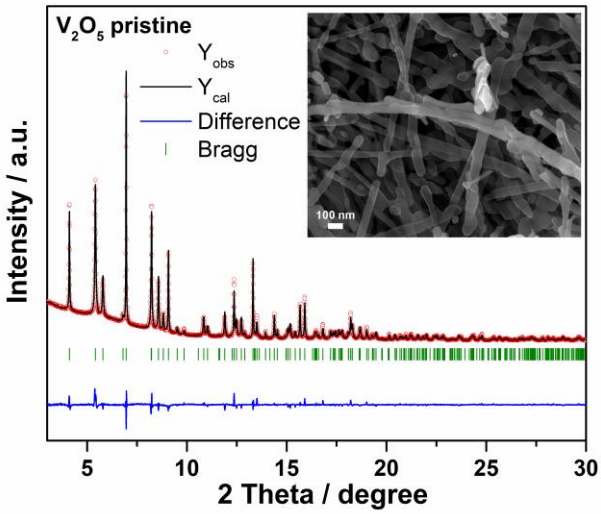

Figure 2 Rietveld refinement from synchrotron diffraction data of V_2O_5 nanowires (inset: SEM image)

The synchrotron diffraction pattern of pristine V_2O_5 nanowires powder is displayed in **Fig. 2**, indicating a high crystallinity of the material. All reflections can be indexed in the orthorhombic α-V_2O_5 structure model with space group *Pmn*2_1, and the lattice parameters are *a*=11.511 Å, *b*=4.373 Å, and *c*=3.565 Å, in accordance with a previously published work[51]. It is quite different from the bilayered $V_2O_5 \cdot nH_2O$[53] that only has few reflections due to its low crystallinity, implying the water-free crystalline V_2O_5 in the present work. SEM (inset in **Fig. 2**) demonstrates that the V_2O_5 is composed of nanowires. The diffraction confirms that the synthesized Mo_6S_8 crystallizes in space group *R* -3 (see **Fig. S2**) with lattice parameters *a*=*b*=9.195 Å, *c*=10.884 Å (hexagonal setting, Bragg R-factor=3.74, R_f-factor=1.81). Two small reflections at 13.34° and 16.99° indicate a very small amount of impurity.

3.2 Electrochemical properties

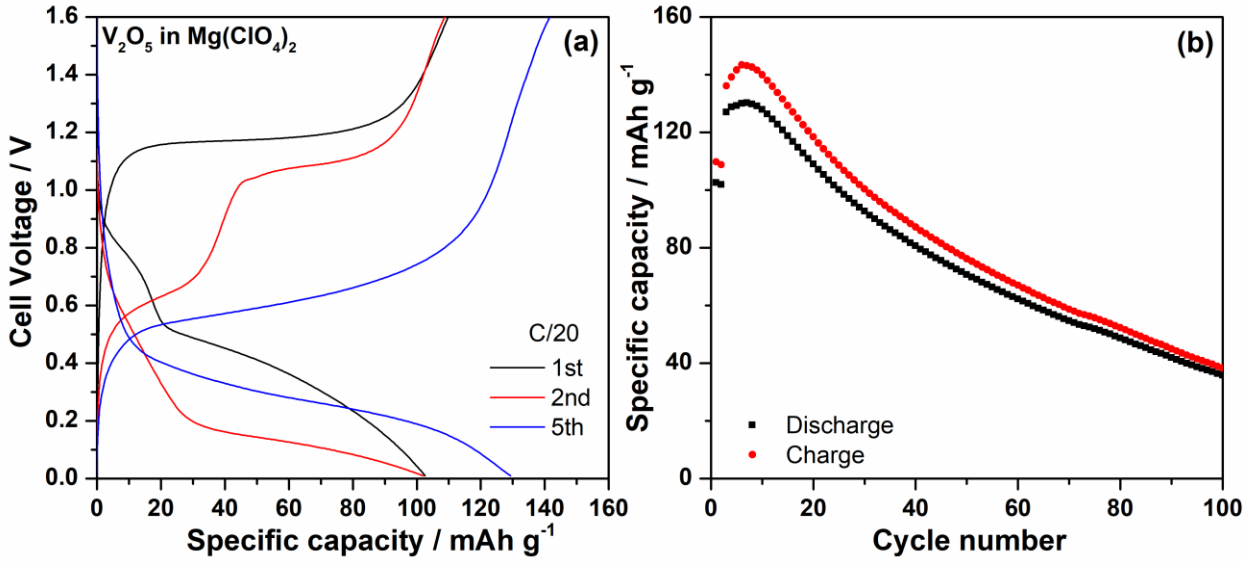

Figure 3 Discharge-charge profiles (a) and cycling performance (b) of V_2O_5 | $Mg(ClO_4)_2$/AN | $Mg_xMo_6S_8$ (x ≈ 2) cell configuration (C/20) in the voltage range of 1.6 - 0.01 V.

Fig. S3 shows the voltage-capacity curve for magnesiation of the Mo_6S_8 electrode in APC electrolyte at C/50. During the 1st discharge, Mo_6S_8 exhibits one plateau at around 0.9 V with a first discharge capacity of 125 mAh g^{-1} (theoretical capacity of 128 mAh g^{-1}), which is in good agreement with previous works[10-11]. **Fig. 3** displays the cycling behavior of V_2O_5 electrode in a cell configuration with $Mg(ClO_4)_2$/AN electrolyte at C/20. During the 1st discharge, a short

plateau at around 0.9 V and a long plateau at around 0.4 V are observed. In contrast, only one flat plateau appears at about 1.1 V for the 1st charge process. V_2O_5 delivers an initial discharge/charge capacity of 103 mAh g^{-1} (0.35 Mg^{2+})/110 mAh g^{-1} and the highest discharge capacity of 130 mAh g^{-1} in the 6th cycle. The cell exhibits a similar discharge capacity of 102 mAh g^{-1} in the second discharge with a lower plateau compared with that of the 1st discharge. Since the capacity or the amount of Mg-ion insertion not only depends on the plateau but also depends on the working voltage range, it shows a capacity increase in the following few cycles at C/20, and after 100 cycles, the cell still delivers a capacity of 36 mAh g^{-1} as shown in **Fig. 3b**. The possible reason responsible for capacity decay could be attributed to unwanted side reaction[54], for example, the dissolution of electrode materials V_2O_5[55-56], a small contribution of structural irreversibility of V_2O_5. The "capacity match" between cathode and anode materials might also play an important role in an "unideal state"[54]. However, understanding the cause of capacity fading with cycling is rather complicated for current operating cell configuration. The real reason responsible for the significant capacity decrease with cycling is required to be understood in the future and it can be the object of the following paper. In the present work, the current density of the C/20 rate is around 14.73 mA g^{-1}, suggesting that the $Mg_xMo_6S_8$ could easily provide enough Mg-ions for the intercalation into the V_2O_5 host structure. This indicates fast kinetics and good rate capability for $Mg_xMo_6S_8$[7, 10]. Moreover, the 10-15 % excess capacity of $Mg_xMo_6S_8$ could provide enough Mg-ions for all V_2O_5 particles based on 1 Mg-ion insertion per formula unit. The voltage profiles of the cell configuration are determined by the curves of V_2O_5 and $Mg_xMo_6S_8$ in half-cells. As the state of charge x in the $Mg_xMo_6S_8$ anode is different for the investigated cell-configurations, different voltage profiles are observed in spite of the same initial V_2O_5 electrodes. This difference could be caused by the different capacity ratio between cathode and anode materials and the different polarizations resulting from different C rates employed. However, the reaction mechanism of V_2O_5 would be expected to be the same despite the observation of different voltage profiles when a similar amount of Mg-ions is inserted into the same V_2O_5 electrode. One has to note that the plateaus cannot be easily distinguished and assigned since cathode V_2O_5 and anode $Mg_xMo_6S_8$ materials have their peculiar electrochemistry characteristics in the cell-configuration system. In our case, sluggish Mg-ion solid diffusion cannot be avoided despite V_2O_5 nanowires, but the electrochemical performance can be improved because of their high reaction areas and short Mg-ion migration pathways of the V_2O_5

nanowires. We suppose a serious capacity degradation of the cell at higher C rates due to the sluggish Mg-ion solid diffusion. Although the charge/discharge rate of C/20 is too slow for the practical application, it is suitable using such slow rate of C/20 to demonstrate that the cell configuration can work with such configuration and, therefore, **can be used for analyzing V_2O_5 through *in operando* techniques**.

3.3 Electrochemical mechanism

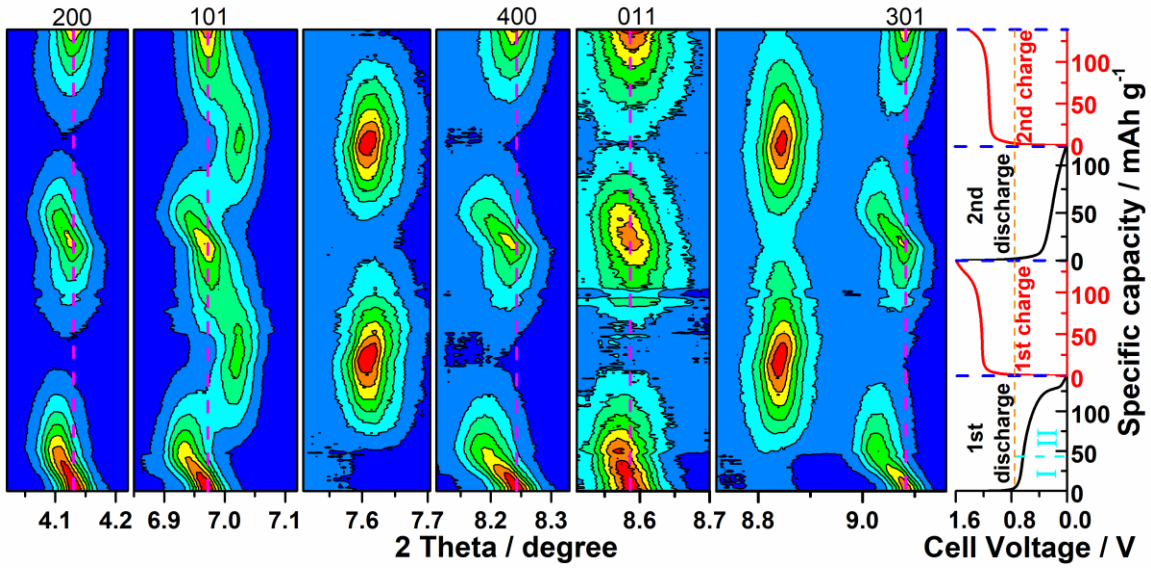

Figure 4 Contour maps of *in operando* synchrotron diffraction of V_2O_5 collected during the first two discharge-charge processes and the corresponding discharge-charge profiles at C/25 at a cell voltage of 0.01 - 1.6 V

In operando synchrotron diffraction was performed to clarify the electrochemical mechanism during the Mg ions insertion and extraction in V_2O_5. Contour maps in the selected ranges during the first two cycles are shown in **Fig. 4**. At the initial stage of discharge, all the reflections could be indexed based on an orthorhombic α-V_2O_5 phase with space group *Pmn*2_1 (see the Rietveld refinement of pristine V_2O_5 in **Fig. S4a**). In the beginning of the 1st discharge (Mg insertion), most reflections of V_2O_5 gradually shift to lower angles, indicating a solid solution process with an expansion of the unit cell (**Region I**). The Mg content of the Mg-poor phase at the end of the solid solution regime was estimated as $Mg_{0.14}V_2O_5$ with lattice parameters of a=11.616 Å, b=4.369 Å, and c=3.591 Å, according to the diffraction patterns and corresponding electrochemical profile (see the Rietveld refinement of $Mg_{0.14}V_2O_5$ in **Fig. S4b**, pattern 21st). Some new reflections appear at 3.8°, 5.7°, 7.0°, 7.6°, 8.84°, 11.4°, 11.65°, 13.5°, 14.94°, and

15.99° when the composition is $Mg_{0.143}V_2O_5$, with a capacity of 42 mAh g^{-1}. The intensities of these new reflections increase, while those from the $Mg_{0.14}V_2O_5$ phase decrease and do not disappear completely at the end of discharge (See **Fig. S5**). Therefore, in the composition range of $Mg_{0.143}V_2O_5$ to $Mg_{0.49}V_2O_5$ (Mg in total 0.49 at 0.01V), a two-phase transition between $Mg_{0.14}V_2O_5$ and a new phase with higher Mg-content occurs (**Region II**). The appearing phase also has an orthorhombic structure with a space group $Pmn2_1$ as the pristine V_2O_5, but with different lattice parameters. This two-phase transition process was not finished at the end of discharge at 0.01 V due to the limited capacity of 144 mAh g^{-1} in the cell configuration. For the Mg-rich phase ($Mg_xV_2O_5$), x was estimated as 0.6 with lattice parameters of a=12.503 Å, b=4.181 Å, and c=3.523 Å, according to the Rietveld refinement and the corresponding electrochemical profile (see the Rietveld refinement based on pattern 70th in **Fig. S4c**). In the very beginning of the 1st charge process, the intensities of the reflections from the Mg-rich $Mg_xV_2O_5$ phase slightly increase, which might be a delay of the structural response, because of the slow Mg^{2+} diffusion inside the electrode materials. Then, the intensities of the Mg-rich $Mg_xV_2O_5$ phase gradually decrease, while those intensities of the phase with lower Mg content grow up. The positions of the reflections remain at slightly lower 2theta values than that for the initial state. This small unit cell expansion indicates either some residual Mg in the host structure or an irreversible transformation, for example, due to a minor oxygen loss. However, the reflections from the Mg-rich $Mg_xV_2O_5$ phase still exist at the end of the 1st charge (see **Fig. S4d**), which might be correlated to the small irreversible capacity. For the second discharge, the evolution of the reflections is very much resembling what is observed for the first discharge, suggesting that the same mechanism remains active during the second and successive cycles. In contrast, the reflections return back to the initial positions of pristine V_2O_5 and a single phase is obtained at the end of the 2nd charged state at 1.4 V (not reach 1.6 V due to the limited beamtime), indicating the high reversibility of the V_2O_5 material during Mg insertion/extraction (see **Fig. S4e**). Note that the ratio of V and O is constantly 2:5 in the chemical formula, $Mg_xV_2O_5$, in spite of the existence of minor V^{3+} and minor residual from the surfactant symmetric triblock copolymer P123 (confirmed by XPS), as well as the possible dissolution of V ions into the solvent or decomposition of V_2O_5.

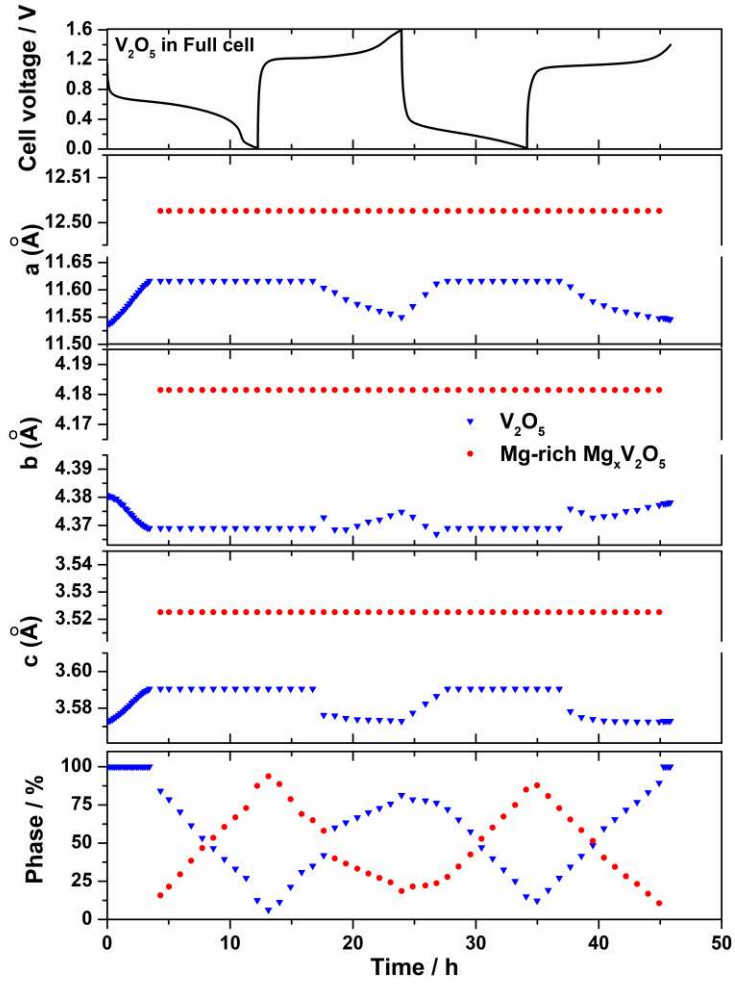

Figure 5 The structural parameters and phases ratios from chosen diffraction patterns with Rietveld refinement during the first two cycles for V_2O_5

The structural parameters and phases ratios are displayed in **Fig. 5**. At the beginning of the first discharge, the phase V_2O_5 accommodates Mg-ions via a solid solution mechanism up to a limiting stoichiometry of $Mg_{0.14}V_2O_5$ accompanied by an increase of lattice parameters *a* and *c* and a decrease of lattice parameter *b*. After that, magnesium uptake goes through a two-phase region with the decrease of the $Mg_{0.14}V_2O_5$ amount and an increase of Mg-rich $Mg_{0.6}V_2O_5$ phase with constant cell parameters for both phases. The phase ratio of $Mg_{0.14}V_2O_5$:$Mg_{0.6}V_2O_5$ is 13:87 at the end of 1st discharge. In the 1st charge process, the material exhibits first a two-phase transition and then a solid solution together with a two-phase transition (the decrease of *a* and *c*, the increase of *b*). In the second cycle, the material shows the same behavior as observed in the first discharge-charge process, except the slightly different phase contribution of both phases at the end of 2nd discharge ($Mg_{0.14}V_2O_5$:$Mg_{0.6}V_2O_5$ =15:85) and a very short region close to the end

of the 2nd charge. The V_2O_5 material returns back to its original structure at the end of the 2nd charge. However, in our case, the crystal structure for Mg-rich $Mg_xV_2O_5$ does not display the same result as reported for the structures of MgV_2O_5 and $Mg_{0.2}V_2O_5$, where MgV_2O_5 crystallizes in orthorhombic structure with a space group of *Cmcm* and $Mg_{0.2}V_2O_5$ has the same structure as the parent V_2O_5 with similar lattice parameters[57-58]. In addition, first-principles calculations, in which a δ-phase (space group: *Cmcm*) presuppose a better mobility for Mg diffusion[59], are not supported by our experimental results either. Meanwhile, first-principles calculations also illustrate that an ε-phase[59], with a specific ordering of Mg-ions at half magnesiated α-V_2O_5 host, is the most stable configuration in the α host and is somehow in agreement with our result, like Li-ordering is discovered in Li-V_2O_5 system[32, 59], as well as has Li-ions at alternate locations along with a-axis[60]. Recently, Xiao et al.[61] reported that V_2O_5 goes through a phase-transition of α-phase into ε-phase and then δ-phase in turn upon Mg insertion ($0 \rightarrow 0.5 \rightarrow 1$) using first-principles calculations. In the Li-V_2O_5 system, it is well known that a topotactic reaction is observed during lithium insertion into V_2O_5 ($0 < x < 1$)[62], where "topotactic" is used to describe that the basic structure of the positive electrode material is maintained during the reaction. The structure of ε-$Li_{0.46}V_2O_5$ (*a*=11.417 Å, *b*= 3.565 Å, and *c*=4.508 Å) has been identified and is very close to that of α-V_2O_5[60]. The newly observed $Mg_{0.6}V_2O_5$ phase (*a*=12.503 Å, *b*=4.181 Å, and *c*=3.523 Å) can also be called ε-$Mg_{0.6}V_2O_5$ phase since the basic structure of the pristine V_2O_5 material is maintained, although the differences in the lattice parameters are more pronounced. However, an increase of the interplanar spacing and a decrease of lattice parameter *a* were observed during the lithiation of α-V_2O_5[60], different from a decrease of the interplanar distance and an increase of lattice parameter *a* as obtained during magnesiation of α-V_2O_5 (**Region I** in **Fig. 4**). This is attributed to the larger charge and smaller radii of Mg^{2+} in the host structure V_2O_5, compressing the layer and extending the *a* direction.

In order to probe the electronic and structural environments of V-ions during the electrochemical process, *in operando* X-ray absorption spectroscopy was performed on the V_2O_5 cathode material in an *in operando* coin cell. For the V K-edge, XAS spectra of V_2O_5, VO_2, and V_2O_3, where the V-ions exist in +5, +4, and +3 oxidation states, respectively, are used as standard materials. The edge position of XAS spectra measured at different electrochemical potentials is compared with reference spectra, where the x values of $Mg_xV_2O_5$ were determined from the charge and capacity in the electrochemical data recorded by EC lab software for each spectrum.

As demonstrated in **Fig. 6**, in terms of V K-edge, the edge position of the XAS spectrum, corresponding to the initial state, is slightly lower than that of V_2O_5 reference. Therefore, the oxidation state of V can be confirmed to be mainly +5 in the initial state, which is in agreement with the XPS result for pristine V_2O_5 (**Fig. 8**). In addition, an intense pre-edge peak on XANES data for V K-edge of pristine V_2O_5 is observed, which is attributed to the transitions between the 1s and bound p-hybridized d-states[63-64] when the centrosymmetric character of V site is lost. This is because the crystal structure of V_2O_5 is orthorhombic, made of [VO_5] square pyramids layers by sharing edges and corners, and the V-ions are five-fold coordinated by oxygens in a distorted tetragonal pyramid.

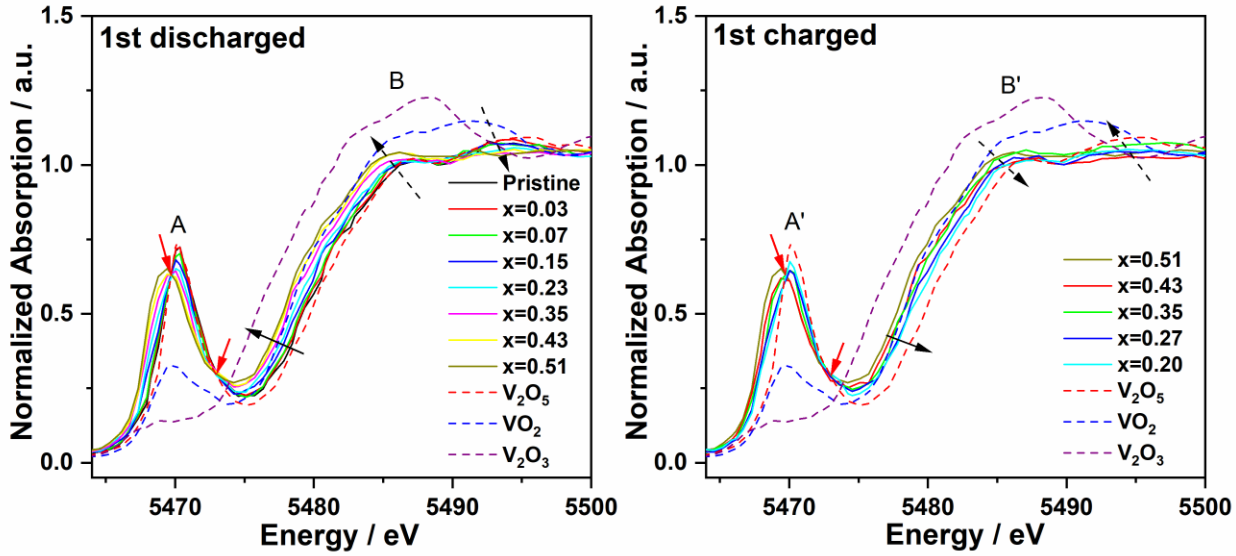

Figure 6 *In operando* X-ray absorption near edge spectroscopy (XANES) for V K-edge during the first discharge-charge process; the isosbestic points are indicated by red arrows.

During the discharging process, the edge position of the V K-edge progressively shifts to lower energy, indicating the reduction of vanadium ions, which attributes to the increase of inserted Mg^{2+} ions into V_2O_5. This is consistent with the electrochemical data (see **Fig. S6**) and XPS result in **Fig. 8**. The edge position of the V K-edge for the electrode discharged to 0.01V (x=0.51 in $Mg_xV_2O_5$) is almost in the middle between that of standard V_2O_3 and V_2O_5, where a similar result was observed for bilayered V_2O_5 after Mg-ion insertion[65]. The pre-edge peak (A in **Fig. 6**) also gradually shifts to lower energy and becomes broad, while the pre-edge peak intensity progressively reduces, suggesting the vanadium ions' reduction and the deformation of the local V environments during Mg^{2+} insertion. The broadness of the pre-edge peak is attributed to co-

existence of distorted tetragonal pyramid and centrosymmetric VO_6 octahedral. The edge resonance (B and B' in **Fig. 6**) displays significant changes in both shape and intensity, which is associated with the energy absorption by core electrons[64, 66]. For the discharging process, the shape changes from two broad peaks to a single broad peak (peak B in **Fig. 6**) and the intensity of one peak at around 5486 eV slightly increases while the other one at around 5493 eV slightly decreases. Moreover, two distinct isosbestic points[67] (red arrows in **Fig. 6**) are detected at both high and low energy for discharge and charge processes, indicating the two-phase along with the Mg ions insertion into and extraction from V_2O_5. For the charging process, the edge position of V K-edge shows a reversible behavior with a shift to higher energy, indicating the oxidation of V in the material. The pre-edge peak and edge resonance (A' and B' in **Fig. 6**) also display reversible behavior compared with that of the discharging process. However, unfortunately, the recording of the charging process is not complete due to a beam loss during the experiment at the beamline.

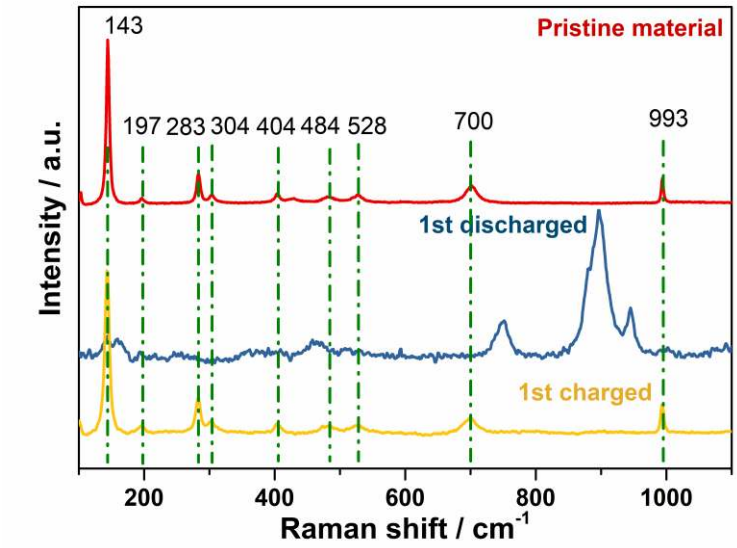

Figure 7 Raman spectrum of pristine V_2O_5, 1st discharged V_2O_5, and 1st charged V_2O_5

To study the local structure of the samples, Raman scattering was carried out as shown in **Fig. 7**. As known in the pristine orthorhombic V_2O_5, oxygen atoms occupy four types of sites in a [VO_5] slab, denoted as O(1)–O(4). The stretching mode of the V–O(1) bond is located at 993 cm^{-1} while its bending vibrations are located at 404 and 283 cm^{-1}. Raman peaks at 484 cm^{-1} and 700 cm^{-1} are attributed to the V–O(2) bending vibration and the V–O(3) stretching vibration, respectively. The peaks at 528 and 304 cm^{-1} are assigned to the V–O(4) bond stretching and

bending vibrations, respectively. The peaks at lower wavenumbers, 143 and 197 cm^{-1} are because of a weak van der Waals interaction between neighboring [VO_5] slabs. These results are highly consistent with previous work[28, 68]. After Mg^{2+} is inserted, significant changes can be obtained and some peaks from V_2O_5 become weak such as 993 and 143 cm^{-1}, while those at 700, 528, 304, and 283 cm^{-1} completely disappear. Meanwhile, some broad new peaks appear at 159, 246, 360, 460, 509, 751, 896, and 945 cm^{-1}. Similarly, significant changes via *in operando* Raman study are also obtained for V_2O_5 during Li-insertion in the range of $0 < x < 1.0$ ($Li_xV_2O_5$)[68]. Therefore, these new peaks might be attributed to the new phase of ε-$Mg_{0.6}V_2O_5$, where the broad peaks are probably ascribed to the disordered local structure in the ε-$Mg_{0.6}V_2O_5$ phase. A broad peak centered at 900 cm^{-1} is also obtained for $Mg_{0.5}V_2O_5$ in Gershinsky's work[28]. It can be deduced that Mg^{2+} ions are inserted into the interlayer of V_2O_5 crystals and bonded with oxygen atoms ([MgO_6] octahedra) in the V_2O_5 structure to form the Mg-rich $Mg_xV_2O_5$ phase. After charging, new peaks observed in the discharged state disappear and those peaks from V_2O_5 return back to the initial state. These results indicate that the Mg^{2+} insertion leads to the formation of $Mg_{0.6}V_2O_5$ phase and Mg extraction returns the Mg-rich material to initial V_2O_5 structure as derived from *in operando* synchrotron diffraction.

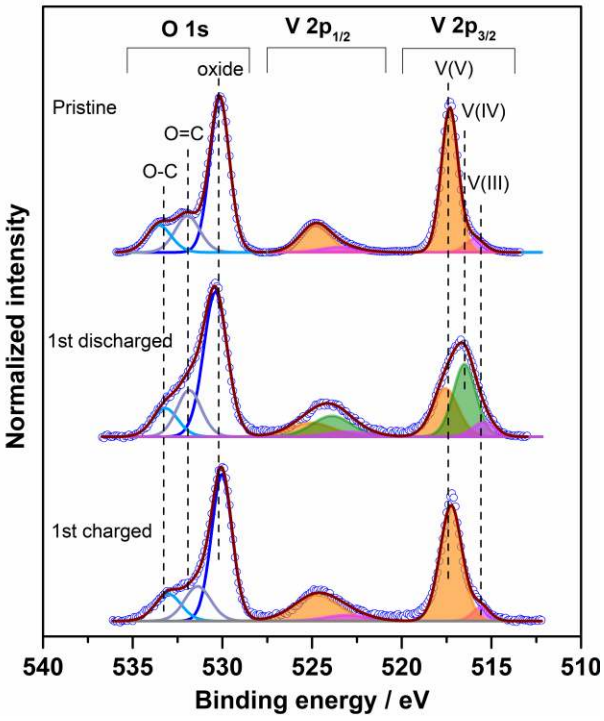

Figure 8 V 2p and O1s X-ray photoelectron spectra of pristine V_2O_5, 1st discharged V_2O_5, and 1st charged V_2O_5

X-ray photoelectron spectroscopy (XPS) was utilized to look into the surface chemistry and surface elemental composition of pristine V_2O_5, 1st discharged V_2O_5, and 1st charged V_2O_5 (XPS survey spectra of three materials see **Fig. S7**). According to **Fig. 8**, the V 2p spectrum of pristine V_2O_5 can be fitted with two doublets: a main one with V $2p_{3/2}$ at 517.2 eV and a second one with weak intensity at 515.7 eV[69], which indicates that V exists mainly in the oxidation state +5 with a minor contribution of vanadium in +3. It can be seen that the O 1s spectrum of pristine V_2O_5 can be fitted with 3 peaks at 533.6 eV, 532.0 eV, and 530.1 eV, which correspond to the O-C and O=C, as well as V-O groups[70-72]. O=C and O-C could be attributed to the residual surfactant symmetric triblock copolymer P123 during synthesis while the minor V(III) could be assigned to the reduction of residual surfactant P123 during the annealing at 400 °C. The V 2p spectrum in the discharged state could be fitted with 3.6 at% V(IV) at 516.7 eV, 2.6 at% V(V) at 517.3 eV, and 0.7 at% V(III) at 515.7 eV, while the V 2p spectrum of charged state displays two V $2p_{3/2}$ components at 517.3 eV and 515.7 eV, returning back to the spectrum of pristine V_2O_5, with 5.9 at% V(V) and 0.6 at% V(III). Therefore, ~60 % of V(V) was reduced to V(IV) during the electrochemical discharge and then again fully oxidized upon electrochemical charging, which is consistent with the electrochemical data (x=0.62 in $Mg_xV_2O_5$).

4. Conclusion

In conclusion, the orthorhombic V_2O_5 nanowires were successfully synthesized via a hydrothermal approach. In the V_2O_5 | $Mg(ClO_4)_2$/AN | $Mg_xMo_6S_8$ cell configuration, the V_2O_5 nanowires obtain an initial discharge/charge capacity of 103 mAh g^{-1}/110 mAh g^{-1} and the highest discharge capacity of 130 mAh g^{-1} in the 6th cycle at a C/20 rate. The reversibility of the magnesium insertion/extraction in the V_2O_5 is clarified through *in operando* synchrotron diffraction and *in operando* XAS together with *ex situ* Raman and XPS. *In operando* synchrotron diffraction and *ex situ* Raman revealed the formation of a new phase of Mg-rich $Mg_xV_2O_5$ during Mg insertion and the recovery of V_2O_5 during Mg extraction. *In operando* XAS and *ex situ* XPS confirmed the reduction/oxidation of vanadium during the Mg insertion/extraction. It is the first time that the structural evolution and charge compensation mechanisms of Mg insertion into V_2O_5 in an electrochemical cell configuration are elucidated through *in operando* synchrotron

diffraction and *in operando* XAS. This will pave the way to study the mechanism of electrode materials not only within the Mg-based batteries but also within other various different challenging systems.

Acknowledgments

This work contributes to the research performed at CELEST (Center for Electrochemical Energy Storage Ulm-Karlsruhe) and is funded by the Deutsche Forschungsgemeinschaft (DFG, German Research Foundation) under Germany´s Excellence Strategy – EXC-2154/1 – Project A.2.1. Our research work has gained benefit from beamtime allocation at BL04 - MSPD at ALBA Synchrotron, Barcelona, Spain, at the XAS beamline Synchrotron at the KIT, Karlsruhe, and at PETRA-III beamline P65 at DESY, Hamburg, Germany. We express our heartfelt thanks to Dr. Aleksandr Missiul of Experiments Division at ALBA. Bettina Hunzinger is also thanked because of the SEM measurement. The K-Alpha$^+$ instrument was supported by the German Federal Ministry of Economics and Technology (grant 03ET6040) based on a decision by the German Bundestag.

Additional information

Supplementary Information is available free of charge on the ACS Publications website at DOI.

Fig. S1-S7.

References

1. Etacheri, V.; Marom, R.; Elazari, R.; Salitra, G.; Aurbach, D., Challenges in the development of advanced Li-ion batteries: a review. *Energy & Environmental Science* **2011,** *4* (9), 3243-3262.
2. Jeong, G.; Kim, Y.-U.; Kim, H.; Kim, Y.-J.; Sohn, H.-J., Prospective materials and applications for Li secondary batteries. *Energy & Environmental Science* **2011,** *4* (6), 1986-2002.
3. Larcher, D.; Tarascon, J. M., Towards greener and more sustainable batteries for electrical energy storage. *Nature Chemistry* **2015,** *7* (1), 19-29.
4. Whittingham, M. S., Lithium Batteries and Cathode Materials. *Chemical Reviews* **2004,** *104* (10), 4271-4302.
5. Muldoon, J.; Bucur, C. B.; Gregory, T., Quest for Nonaqueous Multivalent Secondary Batteries: Magnesium and Beyond. *Chemical Reviews* **2014,** *114* (23), 11683–11720.
6. Saha, P.; Datta, M. K.; Velikokhatnyi, O. I.; Manivannan, A.; Alman, D.; Kumta, P. N., Rechargeable magnesium battery: Current status and key challenges for the future. *Progress in Materials Science* **2014,** *66*, 1-86.
7. Yoo, H. D.; Shterenberg, I.; Gofer, Y.; Gershinsky, G.; Pour, N.; Aurbach, D., Mg rechargeable batteries: an on-going challenge. *Energy & Environmental Science* **2013,** *6* (8), 2265-2279.

8. Keyzer, E. N.; Glass, H. F. J.; Liu, Z. G.; Bayley, P. M.; Dutton, S. E.; Grey, C. P.; Wright, D. S., $Mg(PF_6)_2$-Based Electrolyte Systems: Understanding Electrolyte-Electrode Interactions for the Development of Mg-Ion Batteries. *Journal of the American Chemical Society* **2016,** *138* (28), 8682-8685.
9. Gregory, T. D.; Hoffman, R. J.; Winterton, R. C., Nonaqueous Electrochemistry of Magnesium Applications to Energy Storage. *J. Electrochem. Soc.,* **1990,** *137*, 775-780.
10. Aurbach, D.; Lu, Z.; Schechter, A.; Gofer, Y.; Gizbar, H.; Turgeman, R.; Cohen, Y.; Moshkovich, M.; Levi, E., Prototype systems for rechargeable magnesium batteries. *Nature* **2000,** *407* (6805), 724-727.
11. Mizrahi, O.; Amir, N.; Pollak, E.; Chusid, O.; Marks, V.; Gottlieb, H.; Larush, L.; Zinigrad, E.; Aurbach, D., Electrolyte solutions with a wide electrochemical window for recharge magnesium batteries. *Journal of the Electrochemical Society* **2008,** *155* (2), A103-A109.
12. Cheng, Y.; Liu, T.; Shao, Y.; Engelhard, M. H.; Liu, J.; Li, G., Electrochemically stable cathode current collectors for rechargeable magnesium batteries. *Journal of Materials Chemistry A* **2014,** *2* (8), 2473-2477.
13. Xu, K., "Charge-Transfer" Process at Graphite/Electrolyte Interface and the Solvation Sheath Structure of Li^+ in Nonaqueous Electrolytes. *Journal of The Electrochemical Society* **2007,** *154* (3), A162-A167.
14. Lapidus, S. H.; Rajput, N. N.; Qu, X.; Chapman, K. W.; Persson, K. A.; Chupas, P. J., Solvation structure and energetics of electrolytes for multivalent energy storage. *Physical Chemistry Chemical Physics* **2014,** *16* (40), 21941-21945.
15. Novak, P.; Imhof, R.; Haas, O., Magnesium insertion electrodes for rechargeable nonaqueous batteries - a competitive alternative to lithium? *Electrochimica Acta* **1999,** *45* (1-2), 351-367.
16. Sun, Y.; Zhang, L.; Wang, S.; Lieberwirth, I.; Yu, Y.; Chen, C., Walnut-like vanadium oxide film with high rate performance as a cathode material for rechargeable lithium batteries. *Journal of Power Sources* **2013,** *228*, 7-13.
17. Tang, P. E.; Sakamoto, J. S.; Baudrin, E.; Dunn, B., V_2O_5 aerogel as a versatile host for metal ions. *Journal of Non-Crystalline Solids* **2004,** *350*, 67-72.
18. Novák, P.; Scheifele, W.; Joho, F.; Haas, O., Electrochemical Insertion of Magnesium into Hydrated Vanadium Bronzes. *Journal of The Electrochemical Society* **1995,** *142* (8), 2544-2550.
19. Le, D. B.; Passerini, S.; Coustier, F.; Guo, J.; Soderstrom, T.; Owens, B. B.; Smyrl, W. H., Intercalation of Polyvalent Cations into V_2O_5 Aerogels. *Chemistry of Materials* **1998,** *10* (3), 682-684.
20. Yu, L.; Zhang, X. G., Electrochemical insertion of magnesium ions into V_2O_5 from aprotic electrolytes with varied water content. *Journal of Colloid and Interface Science* **2004,** *278* (1), 160-165.
21. Kim, R.-H.; Kim, J.-S.; Kim, H.-J.; Chang, W.-S.; Han, D.-W.; Lee, S.-S.; Doo, S.-G., Highly reduced VO_x nanotube cathode materials with ultra-high capacity for magnesium ion batteries. *Journal of Materials Chemistry A* **2014,** *2*, 20636-20641.
22. Lee, S. H.; DiLeo, R. A.; Marschilok, A. C.; Takeuchi, K. J.; Takeuchi, E. S., Sol Gel Based Synthesis and Electrochemistry of Magnesium Vanadium Oxide: A Promising Cathode Material for Secondary Magnesium Ion Batteries. *Ecs Electrochemistry Letters* **2014,** *3* (8), 87-90.
23. Imamura, D.; Miyayama, M.; Hibino, M.; Kudo, T., Mg intercalation properties into V_2O_5 gel/carbon composites under high-rate condition. *Journal of the Electrochemical Society* **2003,** *150* (6), A753-A758.
24. Andrews, J. L.; Mukherjee, A.; Yoo, H. D.; Parija, A.; Marley, P. M.; Fakra, S.; Prendergast, D.; Cabana, J.; Klie, R. F.; Banerjee, S., Reversible Mg-Ion Insertion in a Metastable One-Dimensional Polymorph of V_2O_5. *Chem* **2018,** *4* (3), 564-585.
25. Cheng, Y.; Shao, Y.; Raju, V.; Ji, X.; Mehdi, B. L.; Han, K. S.; Engelhard, M. H.; Li, G.; Browning, N. D.; Mueller, K. T.; Liu, J., Molecular Storage of Mg Ions with Vanadium Oxide Nanoclusters. *Advanced Functional Materials* **2016,** *26* (20), 3446-3453.

26. Drosos, C.; Jia, C.; Mathew, S.; Palgrave, R. G.; Moss, B.; Kafizas, A.; Vernardou, D., Aerosol-assisted chemical vapor deposition of V_2O_5 cathodes with high rate capabilities for magnesium-ion batteries. *Journal of Power Sources* **2018,** *384*, 355-359.
27. Sa, N. Y.; Wang, H.; Proffit, D. L.; Lipson, A. L.; Key, B.; Liu, M.; Feng, Z. X.; Fister, T. T.; Ren, Y.; Sun, C. J.; Vaughey, J. T.; Fenter, P. A.; Persson, K. A.; Burrell, A. K., Is alpha-V_2O_5 a cathode material for Mg insertion batteries? *Journal of Power Sources* **2016,** *323*, 44-50.
28. Gershinsky, G.; Yoo, H. D.; Gofer, Y.; Aurbach, D., Electrochemical and Spectroscopic Analysis of Mg2+Intercalation into Thin Film Electrodes of Layered Oxides: V_2O_5 and MoO_3. *Langmuir* **2013,** *29* (34), 10964-10972.
29. Herklotz, M.; Scheiba, F.; Hinterstein, M.; Nikolowski, K.; Knapp, M.; Dippel, A.-C.; Giebeler, L.; Eckert, J.; Ehrenberg, H., Advances in in situ powder diffraction of battery materials: a case study of the new beamline P02.1 at DESY, Hamburg. *Journal of Applied Crystallography* **2013,** *46* (4), 1117-1127.
30. Herklotz, M.; Weiss, J.; Ahrens, E.; Yavuz, M.; Mereacre, L.; Kiziltas-Yavuz, N.; Drager, C.; Ehrenberg, H.; Eckert, J.; Fauth, F.; Giebeler, L.; Knapp, M., A novel high-throughput setup for in situ powder diffraction on coin cell batteries. *Journal of Applied Crystallography* **2016,** *49* (1), 340-345.
31. Yao, J.; Li, Y.; Massé, R. C.; Uchaker, E.; Cao, G., Revitalized interest in vanadium pentoxide as cathode material for lithium-ion batteries and beyond. *Energy Storage Materials* **2018,** *11*, 205-259.
32. Delmas, C.; Cognac-Auradou, H.; Cocciantelli, J. M.; Ménétrier, M.; Doumerc, J. P., The $Li_xV_2O_5$ system: An overview of the structure modifications induced by the lithium intercalation. *Solid State Ionics* **1994,** *69* (3), 257-264.
33. Cocciantelli, J. M.; Ménétrier, M.; Delmas, C.; Doumerc, J. P.; Pouchard, M.; Broussely, M.; Labat, J., On the δ → γ irreversible transformation in Li//V_2O_5 secondary batteries. *Solid State Ionics* **1995,** *78* (1), 143-150.
34. Liu, Q.; Liu, Y.; Sun, C.-J.; Li, Z.-f.; Ren, Y.; Lu, W.; Stach, E. A.; Xie, J., The Structural Evolution of V_2O_5 Nanocystals during Electrochemical Cycling Studied Using In operando Synchrotron Techniques. *Electrochimica Acta* **2014,** *136*, 318-322.
35. Palanisamy, K.; Um, J. H.; Jeong, M.; Yoon, W.-S., Porous V_2O_5/RGO/CNT hierarchical architecture as a cathode material: Emphasis on the contribution of surface lithium storage. *Scientific reports* **2016,** *6*, 31275.
36. De Jesus, L. R.; Andrews, J. L.; Parija, A.; Banerjee, S., Defining Diffusion Pathways in Intercalation Cathode Materials: Some Lessons from V_2O_5 on Directing Cation Traffic. *ACS Energy Letters* **2018,** *3* (4), 915-931.
37. Rozier, P.; Savariault, J. M.; Galy, J., A new interpretation of the $Li_xV_2O_5$ electrochemical behaviour for 1<x<3. *Solid State Ionics* **1997,** *98* (3), 133-144.
38. Wang, Z.; Su, Q.; Deng, H., Single-layered V_2O_5 a promising cathode material for rechargeable Li and Mg ion batteries: an ab initio study. *Physical Chemistry Chemical Physics* **2013,** *15* (22), 8705-8709.
39. Zhou, B.; Shi, H.; Cao, R.; Zhang, X.; Jiang, Z., Theoretical study on the initial stage of a magnesium battery based on a V_2O_5 cathode. *Physical Chemistry Chemical Physics* **2014,** *16* (34), 18578-18585.
40. Zhao, X. D.; Zhang, X.; Wu, D. H.; Zhang, H. C.; Ding, F.; Zhou, Z., Ab initio investigations on bulk and monolayer V_2O_5 as cathode materials for Li-, Na-, K- and Mg-ion batteries. *Journal of Materials Chemistry A* **2016,** *4* (42), 16606-16611.
41. Lossius, L. P.; Emmenegger, F., Plating of magnesium from organic solvents. *Electrochimica Acta* **1996,** *41* (3), 445-447.
42. Gofer, Y.; Turgeman, R.; Cohen, H.; Aurbach, D., XPS investigation of surface chemistry of magnesium electrodes in contact with organic solutions of organochloroaluminate complex salts. *Langmuir* **2003,** *19* (6), 2344-2348.

43. Chen, Z.; Qin, Y.; Weng, D.; Xiao, Q.; Peng, Y.; Wang, X.; Li, H.; Wei, F.; Lu, Y., Design and Synthesis of Hierarchical Nanowire Composites for Electrochemical Energy Storage. *Advanced Functional Materials* **2009,** *19* (21), 3420-3426.
44. Lancry, E.; Levi, E.; Mitelman, A.; Malovany, S.; Aurbach, D., Molten salt synthesis (MSS) Of $Cu_2Mo_6S_8$- New way for large-scale production of Chevrel phases. *Journal of Solid State Chemistry* **2006,** *179* (6), 1879-1882.
45. Fauth, F.; Peral, I.; Popescu, C.; Knapp, M., The new Material Science Powder Diffraction beamline at ALBA Synchrotron. *Powder Diffraction* **2013,** *28* (S2), S360-S370.
46. Parry, K. L.; Shard, A. G.; Short, R. D.; White, R. G.; Whittle, J. D.; Wright, A., ARXPS characterisation of plasma polymerised surface chemical gradients. *Surface and Interface Analysis* **2006,** *38* (11), 1497-1504.
47. Scofield, J. H., Hartree-Slater subshell photoionization cross-sections at 1254 and 1487 eV. *J. Electron Spectrosc. Relat. Phenom.* **1976,** *8* (2), 129-137.
48. Tanuma, S.; Powell, C. J.; Penn, D. R., Calculations of electron inelastic mean free paths. V. Data for 14 organic compounds over the 50–2000 eV range. *Surface and Interface Analysis* **1994,** *21* (3), 165-176.
49. Nikolowski, K.; Baehtz, C.; Bramnik, N. N.; Ehrenberg, H., A Swagelok-type in situ cell for battery investigations using synchrotron radiation. *Journal of Applied Crystallography* **2005,** *38*, 851-853.
50. J. Rodríguez-Carvajal, Recent Developments of the Program FULLPROF. *in Commission on Powder Diffraction (IUCr). Newsletter* **2001,** *26*, 12-19.
51. Shklover, V.; Haibach, T.; Ried, F.; Nesper, R.; Novák, P., Crystal Structure of the Product of Mg2+Insertion into V_2O_5 Single Crystals. *Journal of Solid State Chemistry* **1996,** *123* (2), 317-323.
52. Ravel, B.; Newville, M., ATHENA, ARTEMIS, HEPHAESTUS: data analysis for X-ray absorption spectroscopy using IFEFFIT. *Journal of Synchrotron Radiation* **2005,** *12* (4), 537-541.
53. Moretti, A.; Passerini, S., Bilayered Nanostructured $V_2O_5{\cdot}nH_2O$ for Metal Batteries. *Advanced Energy Materials* **2016,** *6* (23), 1600868.
54. Arora, P.; White, R. E.; Doyle, M., Capacity Fade Mechanisms and Side Reactions in Lithium-Ion Batteries. *Journal of The Electrochemical Society* **1998,** *145* (10), 3647-3667.
55. Leger, C.; Bach, S.; Soudan, P.; Pereira-Ramos, J. P., Evaluation of the sol–gel mixed oxide Cr0.11V2O5.16 as a rechargeable positive electrode working in the potential range 3.8/1.5 V vs. Li. *Solid State Ionics* **2005,** *176* (15), 1365-1369.
56. Tang, H.; Peng, Z.; Wu, L.; Xiong, F.; Pei, C.; An, Q.; Mai, L., Vanadium-Based Cathode Materials for Rechargeable Multivalent Batteries: Challenges and Opportunities. *Electrochemical Energy Reviews* **2018,** *1* (2), 169-199.
57. Millet, P.; Satto, C.; Sciau, P.; Galy, J., MgV2O5andδLixV2O5: A Comparative Structural Investigation. *Journal of Solid State Chemistry* **1998,** *136* (1), 56-62.
58. Pereira-Ramos, J. P.; Messina, R.; Perichon, J., Electrochemical formation of a magnesium vanadium bronze $Mg_xV_2O_5$ in sulfone-based electrolytes at 150°C. *Journal of Electroanalytical Chemistry and Interfacial Electrochemistry* **1987,** *218* (1–2), 241-249.
59. Sai Gautam, G.; Canepa, P.; Abdellahi, A.; Urban, A.; Malik, R.; Ceder, G., The Intercalation Phase Diagram of Mg in V_2O_5 from First-Principles. *Chemistry of Materials* **2015,** *27* (10), 3733-3742.
60. Cocciantelli, J. M.; Doumerc, J. P.; Pouchard, M.; Broussely, M.; Labat, J., Crystal chemistry of electrochemically inserted $Li_xV_2O_5$. *Journal of Power Sources* **1991,** *34* (2), 103-111.
61. Xiao, R.; Xie, J.; Luo, T.; Huang, L.; Zhou, Y.; Yu, D.; Chen, C.; Liu, Y., Phase Transformation and Diffusion Kinetics of V_2O_5 Electrode in Rechargeable Li and Mg Batteries: A First-Principle Study. *The Journal of Physical Chemistry C* **2018,** *122* (3), 1513-1521.

62. S.Crouch-Baker; C-K. Huang; Huggins, R. A., Rationalization of the electrochemical behavior of transition metal oxide positive electrode materials at room temperature. *Proc. Electrochem. Soc.* **1988,** *88-6*, 44.
63. Tanaka, T.; Yamashita, H.; Tsuchitani, R.; Funabiki, T.; Yoshida, S., X-ray absorption (EXAFS/XANES) study of supported vanadium oxide catalysts. Structure of surface vanadium oxide species on silica and [gamma]-alumina at a low level of vanadium loading. *Journal of the Chemical Society, Faraday Transactions 1: Physical Chemistry in Condensed Phases* **1988,** *84* (9), 2987-2999.
64. Wong, J.; Lytle, F. W.; Messmer, R. P.; Maylotte, D. H., K-edge absorption spectra of selected vanadium compounds. *Physical Review B* **1984,** *30* (10), 5596-5610.
65. Tepavcevic, S.; Liu, Y.; Zhou, D.; Lai, B.; Maser, J.; Zuo, X.; Chan, H.; Král, P.; Johnson, C. S.; Stamenkovic, V.; Markovic, N. M.; Rajh, T., Nanostructured Layered Cathode for Rechargeable Mg-Ion Batteries. *ACS Nano* **2015,** *9* (8), 8194–8205.
66. Yoo, H. D.; Liang, Y.; Dong, H.; Lin, J.; Wang, H.; Liu, Y.; Ma, L.; Wu, T.; Li, Y.; Ru, Q.; Jing, Y.; An, Q.; Zhou, W.; Guo, J.; Lu, J.; Pantelides, S. T.; Qian, X.; Yao, Y., Fast kinetics of magnesium monochloride cations in interlayer-expanded titanium disulfide for magnesium rechargeable batteries. *Nature communications* **2017,** *8* (1), 339.
67. Liu, X.; Wang, D.; Liu, G.; Srinivasan, V.; Liu, Z.; Hussain, Z.; Yang, W., Distinct charge dynamics in battery electrodes revealed by in situ and operando soft X-ray spectroscopy. *Nature communications* **2013,** *4*, 2568.
68. Baddour-Hadjean, R.; Pereira-Ramos, J. P.; Navone, C.; Smirnov, M., Raman Microspectrometry Study of Electrochemical Lithium Intercalation into Sputtered Crystalline V_2O_5 Thin Films. *Chemistry of Materials* **2008,** *20* (5), 1916-1923.
69. Silversmit, G.; Depla, D.; Poelman, H.; Marin, G. B.; De Gryse, R., Determination of the V2p XPS binding energies for different vanadium oxidation states (V^{5+} to V^{0+}). *J. Electron Spectrosc. Relat. Phenom.* **2004,** *135* (2-3), 167-175.
70. P., L. G.; G., C. D.; D., R. B., XPS O 1s binding energies for polymers containing hydroxyl, ether, ketone and ester groups. *Surface and Interface Analysis* **1991,** *17* (5), 267-272.
71. Zhu, K.; Qiu, H.; Zhang, Y.; Zhang, D.; Chen, G.; Wei, Y., Synergetic Effects of Al^{3+} Doping and Graphene Modification on the Electrochemical Performance of V_2O_5 Cathode Materials. *ChemSusChem* **2015,** *8* (6), 1017-1025.
72. Światowska-Mrowiecka, J.; Maurice, V.; Zanna, S.; Klein, L.; Marcus, P., XPS study of Li ion intercalation in V_2O_5 thin films prepared by thermal oxidation of vanadium metal. *Electrochimica Acta* **2007,** *52* (18), 5644-5653.

Table of contents